

Article

Muscovite $^{40}\text{Ar}/^{39}\text{Ar}$ Age and H-O-S Isotopes of the Shimensi Tungsten Deposit (Northern Jiangxi Province, South China) and Their Metallogenic Implications

Wen-Feng Wei ^{1,2} , Bing Yan ¹, Neng-Ping Shen ^{2,*} , Lei Liu ², Yong Zhang ³ and Xin-Kui Xiang ⁴

¹ Institute of Earth Sciences, Chengdu University of Technology, Chengdu 610059, China; weifenfenghao@163.com (W.-F.W.); yanbing06@cdut.cn (B.Y.)

² State Key Laboratory of Ore Deposit Geochemistry, Institute of Geochemistry, Chinese Academy of Sciences, Guiyang 550081, China; liulei161@mails.ucas.ac.cn

³ School of Earth Sciences, East China University of Technology, Nanchang 330013, China; zhangyong@ecit.cn

⁴ No. 916 Geological Party, Jiangxi Bureau of Geology & Mineral Exploration, Jiujiang 332100, China; ductile@126.com

* Correspondence: Shennengping@vip.gyig.ac.cn

Received: 19 July 2017; Accepted: 31 August 2017; Published: 11 September 2017

Abstract: The Shimensi deposit (Northern Jiangxi, South China) is a recently discovered super-large tungsten deposit. Muscovite $^{40}\text{Ar}/^{39}\text{Ar}$ dating yielded a plateau age of 145.7 ± 0.9 Ma, with normal and inverse isochronal ages being 145.4 ± 1.4 Ma and 145.3 ± 1.4 Ma, respectively. The muscovite $^{40}\text{Ar}/^{39}\text{Ar}$ age, which can represent the mineralization age, coincides well with the published zircon U–Pb ages (143–148 Ma) of the ore-hosting granites, which indicates that the tungsten mineralization was syn-magmatic. The new age reported here confirms that the Shimensi tungsten deposit is part of a large Early Cretaceous (147–136 Ma) tungsten-polymetallic belt in South China. Measured and calculated sulfur isotopic compositions ($\delta^{34}\text{S}_{\text{minerals}} = -3.0\text{‰}$ to 1.1‰ , average -1.3‰ ; $\delta^{34}\text{S}_{\text{H}_2\text{S}} = -4.5\text{‰}$ to $+1.2\text{‰}$, average -1.8‰) of the Shimensi ore-forming fluids indicate that the sulfur was mainly magmatic-derived. The calculated and measured oxygen and hydrogen isotopic compositions ($\delta^{18}\text{O}_{\text{H}_2\text{O}} = 4.1\text{‰}$ to 6.7‰ , $\delta\text{D} = -62.7\text{‰}$ to -68‰) of the ore-forming fluids indicate a dominantly magmatic source with a meteoric water input. Oxygen isotopic modelling of the boiling/mixing processes indicates that the Shimensi tungsten mineralization was caused mainly by fluid mixing of magmatic hydrothermal fluid with meteoric water.

Keywords: Shimensi; tungsten deposit; muscovite Ar-Ar dating; H-O-S stable isotopes; South China

1. Introduction

South China is well endowed with tungsten resources. Previous exploration efforts were concentrated in the Nanling region (especially southern Jiangxi). Recent discoveries of some super-large tungsten deposits in northern Jiangxi have given this region some of the largest tungsten mines (e.g., Dahutang and Zhuxi) in the world [1,2]. Unlike southern Jiangxi, where tungsten mineralization is associated with tin, tungsten mineralization in northern Jiangxi is associated with copper [3]. The origin of the northern Jiangxi W-Cu deposits has been extensively investigated, and various metallogenic models have been proposed [2–9]. For example, Jiang et al. [2] proposed a two-stage metallogenic model: the first and second mineralization stage were likely related to porphyritic granite and fine grained granite and granite porphyry, respectively. During the extreme fractionation of the granitic magma, metals were concentrated in the late magmatic hydrothermal

fluids and finally deposited as giant orebodies via a two-stage magmatism and mineralization process. The ore-fluid circulation model has been proposed, and fluid driving factors are mainly ascribed to temperature and pressure gradients [9].

The Dahutang tungsten ore district is located in the newly delineated North Yangtze Tungsten Belt (NYTB), which is situated to the north of the Nanling W-Sn metallogenic belt (Figure 1a) [14]. The total resource is estimated to be >1 million tons (Mt) of tungsten (0.185%) and 0.65 Mt of copper (0.16%) [5]. Previous exploration mainly focus on wolframite, whereas recent exploration has suggested good potential of veinlet/disseminated scheelite (CaWO₄) mineralization in areas of wolframite mineralization [6].

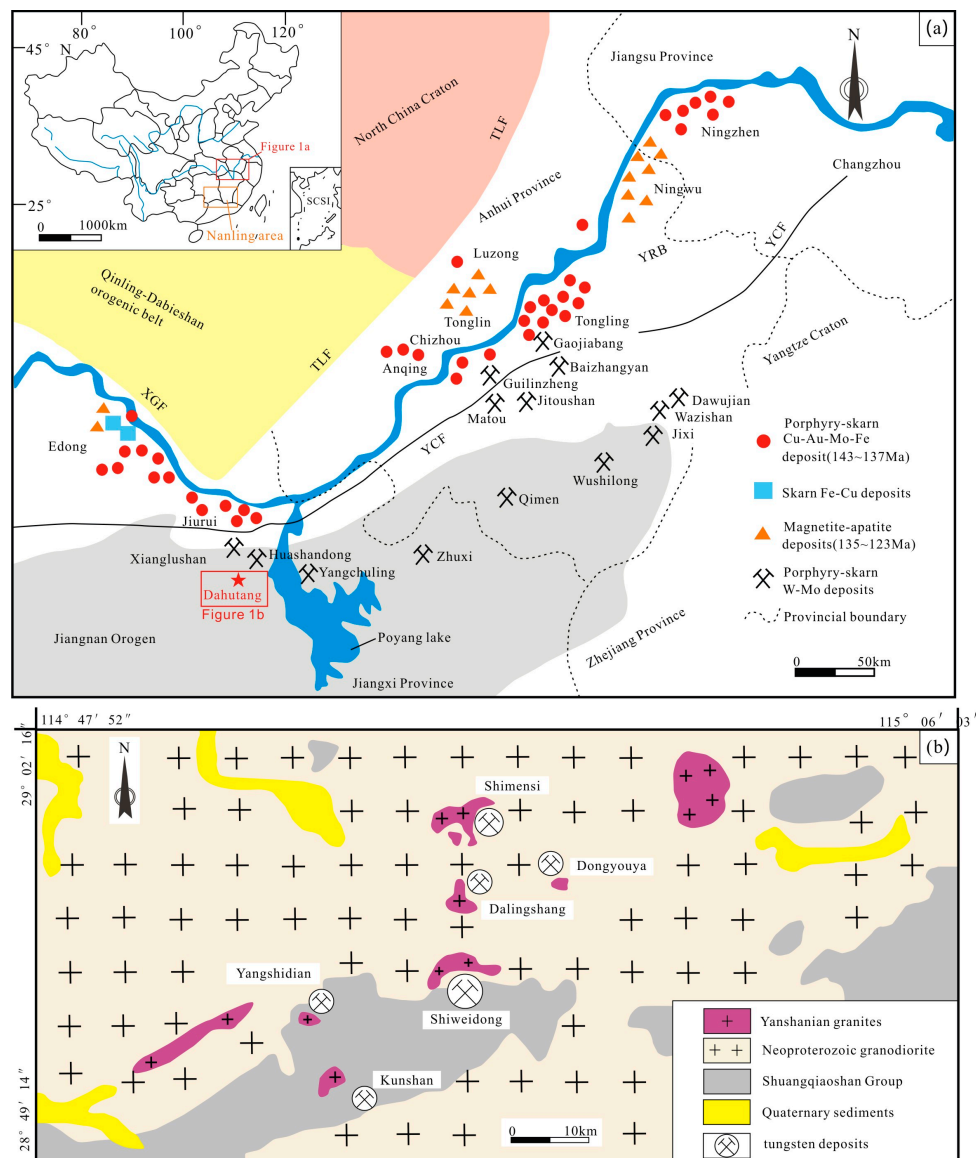


Figure 1. (a) Simplified tectonic map showing major Cu-Au-Mo-Fe porphyry and skarn deposits in the Middle-Lower Yangtze River Metallogenic Belt (MLYRB) and (b) the Dahutang tungsten ore field (modified after [1]). YCF: Yangxing-Changzhou Fault; TLF: Tancheng-Lujiang Fault; XGF: Xiangfan-Guangji Fault.

Preliminary investigations in Shimensi have focused on the local geology and a tentative genetic model [7–13]. The mineralizing fluid was magmatic water [14], but the mixing of two different fluids (e.g., magmatic hydrothermal fluid and meteoric water) was responsible for the

mineralization [13]. The granitic magma is the direct source of tungsten-bearing fluids [1], the sequences of metasedimentary rocks that host the granitic plutons may be another significant metal source [14]. The Re-Os isochron ages of molybdenite vary from 139.2 ± 1.0 to 149.6 ± 1.4 Ma [7,8,15]. Despite previous research, the possible ore-forming fluid sources [1,14] and their interactions in metals transportation, as well as the mineralization age [7,8,15] remain poorly constrained. In this study, we conducted muscovite $^{40}\text{Ar}/^{39}\text{Ar}$ dating and stable isotope (H, O, and S) analyses to address these issues.

2. Geological Background

2.1. Regional Geology

South China includes the Yangtze Block in the northwest and Cathaysia Block in the southeast, and is bordered with the North China Craton in the north and the Tibetan Plateau in the west [16]. The Jiangshan-Shaoxing Fault Zone represents the Yangtze-Cathaysia suture zone that contains widespread ophiolite occurrences [17]. The Dahutang deposit is located in the northern margin of the Yangtze Block. The Middle-Lower Yangtze River Belt (MLYRB) is bounded by several large strike-slip fault systems, including the Xiangfan-Guangji Fault in the northwest, the Tancheng-Lujiang Fault in the northeast and the Yangxing-Changzhou Fault in the south [4]. Exposed rock units in the MLYRB include those of Mesoproterozoic (dominant), Neoproterozoic, Palaeozoic and Mesozoic [6]. Proterozoic rocks in the MLYRB have high tungsten and copper contents, especially in the Jiuling Mountain area (mean W = 9.13 ppm, Cu = 38.1 ppm) [3].

In the Dahutang area, most of the granites were emplaced into the Neoproterozoic granodiorite batholith, and some intruded the Neoproterozoic Shuangqiaoshan Formation greenschist-facies metamorphic rocks (Figure 1b). The Shuangqiaoshan Group comprises thick meta-turbidite sequences, including phyllite, slate, and meta-siltstone [2,12]. Structures (ductile shear zones, fractures and joints) are well-developed in the Dahutang area, and the major ones are mainly EW- or NE-ENE-trending [6]. Local Mesozoic (ca. 150–140 Ma) [8,12] granitoids, e.g., granite, porphyry and granodiorite, occur as small stocks intruding both the Neoproterozoic granodiorite batholiths and Precambrian rocks [4,12].

2.2. Deposit Geology

The Dahutang tungsten ore field contains the Shimensi deposit and five surrounding deposits. Quaternary sediments unconformably overlie Neoproterozoic biotite granodiorite and late Mesozoic granites in the Shimensi area. The late Mesozoic granite stocks and dikes are widespread at Shimensi and are genetically related to the tungsten mineralization [7,8,12]. The tungsten mineralization occurs along the contact between the late Mesozoic granite stocks and the Neoproterozoic granodiorite batholith [8,12]. The late Mesozoic granitic rocks consist predominately of porphyritic biotite granite and fine-grained biotite granite and granite porphyry. The rocks are strongly peraluminous, high-K calc-alkaline, and are classified as highly fractionated S-type granite [4,12]. At Shimensi, a series of EW-striking shear zones is present in the Neoproterozoic biotite granodiorite batholith [18,19]. The best developed NNE-trending faults are steeply SW-dipping, and play a key role in granitoid emplacement and ore formation (Figure 2a) [2,19].

Three mineralization styles are documented in Shimensi ore district (i.e., veinlet-disseminated, quartz vein, and hydrothermal cryptoexplosive breccia), and they commonly co-exist and overprint one another [1,8,10]. The veinlet-disseminated ore bodies are mainly distributed in both the endocontact/exocontact between the Late Mesozoic granite and the Jinningian biotite granodiorite (Figure 2b). This mineralization style is dominated by scheelite and accounts for 74% of total tungsten reserve [18]. The major ore mineral is scheelite, accompanied by small amounts of wolframite, molybdenite, and chalcopyrite, and the gangue minerals are quartz, biotite, muscovite, and fluorite [13,14].

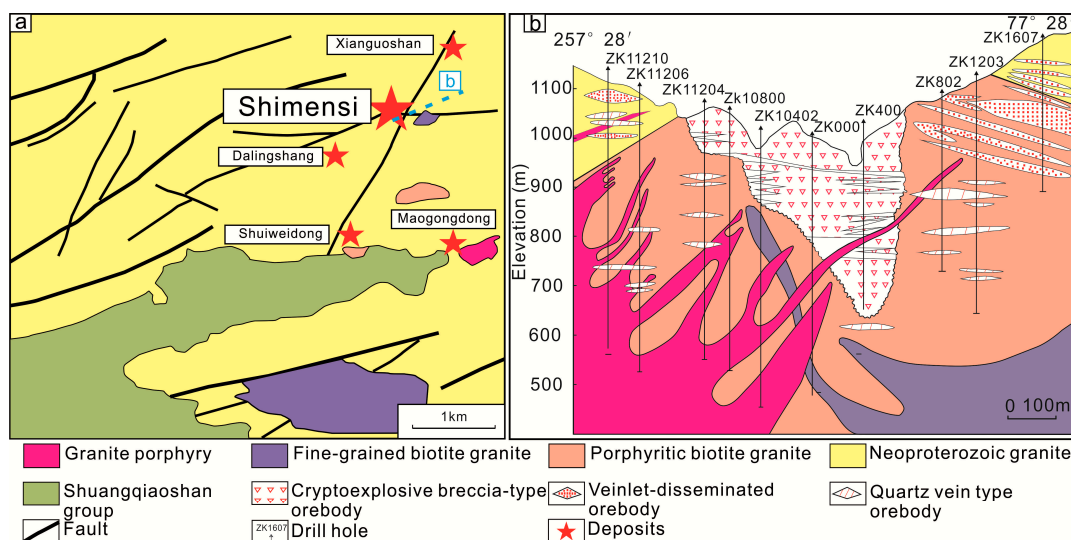


Figure 2. (a) Sketch geological map of the Jiuling Mountains. (b) A NE-trending cross-section of the Shimensi deposit showing three tungsten ore types: veinlets-disseminated, breccia-type, and vein-type mineralization (modified after [19]).

Quartz vein-type ore bodies are mainly distributed in the late Mesozoic porphyritic biotite granite (Figure 2b). Most of the veins trend nearly EW, NNE, and NW. There are more than 60 ore veins at Shimensi. In general, the veins are 200 to 800 m long and 0.2 to 0.7 m thick [2]. Ore minerals include mainly wolframite, chalcopyrite, and molybdenite, with trace amounts of scheelite [10,13]. This mineralization type cross-cuts all the granites and the other two ore types, indicative of being the latest mineralization at Shimensi [14,19].

The hydrothermal cryptoexplosive breccia-type mineralization occurs at the centre of the deposit (Figure 2b). The mineralization is mainly distributed on the top of the porphyritic biotite granite, and in some places extends to the Jinningian biotite granodiorite batholith [2]. The breccias contain porphyritic biotite granite and biotite granodiorite clasts. Ore minerals include mainly scheelite, wolframite, chalcopyrite, and molybdenite, and gangue minerals include quartz, muscovite, K-feldspar, biotite, and fluorite [10,14]. In summary, three mineralization styles contain roughly the same ore mineral types, implying that the ore-forming fluid compositions are approximately similar.

Ore minerals at Shimensi include mainly wolframite, scheelite, chalcopyrite, and molybdenite with minor arsenopyrite, cassiterite, pyrite, and bornite. Gangue minerals are predominately quartz with minor mica and feldspar. The ores have blocky, brecciated, and veinlet-disseminated structures, and euhedral-anhedral granular, metasomatic, and cataclastic textures [1,18]. Hydrothermal alteration is widespread and includes mainly greisen, K-feldspar, silicic, and chlorite alterations [10].

3. Sampling and Analytical Methods

3.1. Muscovite Ar-Ar Dating Method

Muscovite sample (SMS-34) was collected from a muscovite-quartz vein for Ar-Ar dating. The muscovite occurs as euhedral aggregates with a diameter of about 1 to 5 mm. Undeformed mineral separates were handpicked under a binocular microscope. Step-heating $^{40}\text{Ar}/^{39}\text{Ar}$ analyses were performed at the Ar-Ar Laboratory of the Institute of Geology and Geophysics, Chinese Academy of Sciences. The analytical procedures were as described by Wang et al. [20]. Data-processing was performed using ArArCALC 2.4 software [21]. The $^{40}\text{Ar}/^{36}\text{Ar}$ vs. $^{39}\text{Ar}/^{36}\text{Ar}$ isochron diagram was constructed using Isoplot 4.0.

3.2. Stable Isotope

Representative samples (quartz and sulfides) from the Shimensi deposit were chosen for the hydrogen, oxygen, and sulfur isotope analyses. Quartz and sulfides (pyrite, bornite, chalcopyrite, and molybdenite) were separated by careful handpicking under a binocular microscope. Stable isotope analyses were measured at the Stable Isotope Laboratory of the Beijing Geological Research Institute of Nuclear Industry.

Oxygen isotopes of quartz were analysed with the conventional BrF5 method [22]. For hydrogen isotopes, water from fluid inclusions was extracted by heating the samples to ca. 500 °C, and then the water reacted with zinc powder at 410 °C to generate hydrogen [23]. The H and O isotopic compositions were determined using a MAT 251 EM mass spectrometer. All values are reported relative to the V-SMOW standard and the precisions were $\pm 2\%$ and $\pm 0.2\%$ for δD and $\delta^{18}O$, respectively. Sulfur isotope analyses used the continuous flow isotope ratio mass spectrometry. The procedures described by Grassineau et al. [24] were followed in the analysis. The data are reported relative to CDT, and the analytical precision was $\pm 0.2\%$.

4. Analytical Results

4.1. Muscovite Ar-Ar Age

The Ar-Ar isotopic data of muscovite are given in Table 1 and illustrated in Figure 3. In this study, the muscovite was incrementally heated by 13 steps from 700 °C to 1220 °C and yielded a concordant age spectrum. The plateau comprises 13 continuous steps accounting for 98.8% of the released total ^{39}Ar and defined a plateau age of 145.7 ± 0.9 Ma (2σ , MSWD = 0.22), consistent with normal and inverse isochron ages of 145.4 ± 1.4 Ma and 145.3 ± 1.4 Ma, respectively (Figure 3). The spectral characteristics and the initial $^{40}Ar/^{36}Ar$ values of 298.6 ± 6.4 and 298 ± 11 are very close to the atmospheric value (298.6 ± 0.3 , the superior precision measurements determined by Lee et al. [25]). This implies that argon loss or excess argon did not occur or that their influence on the measured age was negligible, i.e., the muscovite system analyzed remained closed during its geological evolution, and thus the Ar-Ar age is reliable.

Table 1. $^{40}Ar/^{39}Ar$ analytical data for muscovite from the Shimensi tungsten deposit, South China.

T (°C)	$(^{40}Ar/^{39}Ar)_m$	$(^{36}Ar/^{39}Ar)_m$	$(^{37}Ar_0/^{39}Ar)_m$	$(^{38}Ar/^{39}Ar)_m$	^{40}Ar (%)	F	^{39}Ar ($\times 10^{-14}$ mol)	^{39}Ar (Cum.) (%)	Age (Ma)	$\pm 1\sigma$ (Ma)
700	94.2546	0.2635	3.4274	0.0727	17.64	16.6767	0.02	0.08	144.0	20.0
770	25.9362	0.0291	0.0093	0.0162	66.79	17.3232	0.23	0.84	149.0	2.5
820	22.9143	0.0201	0.0576	0.0167	74.05	16.9697	0.38	2.15	146.1	1.9
860	22.1199	0.0176	0.1290	0.0166	76.49	16.9215	0.66	4.41	145.7	1.6
900	21.2446	0.0146	0.0235	0.0154	79.69	16.9292	1.70	10.20	145.7	1.5
940	17.9495	0.0038	0.0252	0.0134	93.81	16.8385	3.85	23.31	145.0	1.4
980	17.4116	0.0018	0.0044	0.0130	96.94	16.8793	5.19	41.00	145.3	1.4
1020	17.4304	0.0019	0.0062	0.0130	96.80	16.8734	5.80	60.78	145.3	1.4
1060	17.5796	0.0023	0.0164	0.0131	96.19	16.9102	3.73	73.51	145.6	1.4
1100	17.8003	0.0028	0.0402	0.0133	95.28	16.9599	2.20	81.01	146.0	1.4
1160	17.4189	0.0015	0.0030	0.0129	97.42	16.9693	3.86	94.17	146.1	1.4
1220	17.2956	0.0014	0.0438	0.0131	97.66	16.8919	1.37	98.84	145.4	1.4
1400	18.8968	0.0086	0.3145	0.0154	86.71	16.3887	0.34	100.00	141.3	2.1

4.2. Stable Isotopes

The oxygen and hydrogen isotopic results obtained are given in Table 2. The δD of the fluid inclusions in quartz vary from -62.7% to -68.0% (average -64.8%). Oxygen isotopic compositions of hydrothermal waters in equilibrium with quartz were calculated using an extrapolation of the fractionation formula from Clayton et al. [26]. Since fluid inclusion assemblages (i.e., inclusions with similar vapour-to-liquid ratios and heating behaviour) can provide more reliable information [27], the homogenisation temperatures of fluid inclusion assemblages were determined (Table 2). In general, homogenisation temperatures are lower than the fluid inclusion trapping temperatures during

crystallisation. Consequently, we used the highest homogenisation temperatures to calculate the $\delta^{18}\text{O}_{\text{H}_2\text{O}}$. The calculated oxygen isotopic compositions of the fluids ($\delta^{18}\text{O}$) range from 4.1‰ to 6.7‰ (average 5.5‰).

Table 2. Results of the $\delta^{18}\text{O}$ – δD study from Shimensi (data are relative to V-SMOW).

Sample No.	Mineralization Style	Mineral	δD (‰)	$\delta^{18}\text{O}_{\text{Quartz}}$ (‰)	$\delta^{18}\text{O}_{\text{H}_2\text{O}}$ (‰)	Th (°C)
SMS-10	Quartz vein	Quartz	−68.0	12.1	4.5	262–279
SMS-9	Quartz vein	Quartz	−63.9	12.5	6.3	302–318
SMS-17	Quartz vein	Quartz	−66.1	12.7	5.3	274–285
SMS-5	Quartz vein	Quartz	−63.0	13.6	6.7	281–298
SMS-16	Cryptoexplosion breccia	Quartz	−64.9	12.2	4.1	256–267
SMS-24	Cryptoexplosion breccia	Quartz	−62.7	12.8	6.3	295–311

New and published sulfur isotopic data [13,14] are given in Table 3. In this study, $\delta^{34}\text{S}$ values of sulfides from the different samples range from −3.0‰ to −0.8‰ (average −1.8‰). In combination with published data, the $\delta^{34}\text{S}$ values of sulfides vary in a relatively broad range of −3.0‰ to 1.1‰ (average −1.3‰).

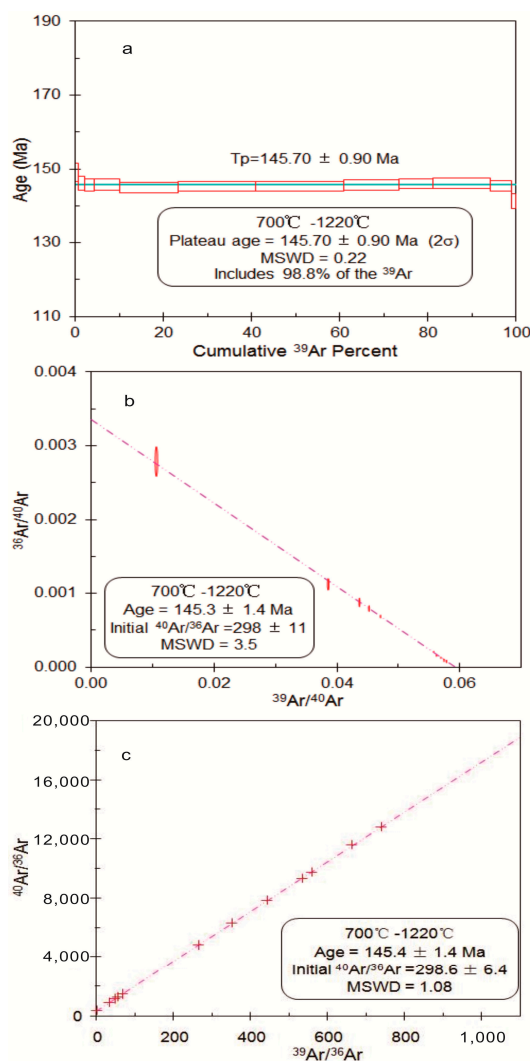


Figure 3. (a) Plateau, (b) inverse and (c) normal isochron muscovite Ar-Ar isotopic age of the Shimensi deposit.

Table 3. Sulfur isotope data from Shimensi (data are relative to V–CDT).

Sample No	Mineralization Style	Mineral	$\delta^{34}\text{S}$ Sulfide ‰	$\delta^{34}\text{S}_{\text{H}_2\text{S}}$ ‰	Data Sources	
SMS-16	Cryptoexplosion breccia	Chalcopyrite	−1.4	−1.2	This study	
SMS-24	Cryptoexplosion breccia	Chalcopyrite	−1.7	−1.6		
SMS-16	Cryptoexplosion breccia	Molybdenite	−2.5	−4.0		
SMS-9	Quartz vein type	Chalcopyrite	−1.4	−1.3		
SMS-10	Quartz vein type	Chalcopyrite	−0.8	−0.6		
SMS-10	Quartz vein type	Molybdenite	−3.0	−4.5		
SMS-17	Quartz vein type	Molybdenite	−1.9	−3.3		
SMS-5	Quartz vein type	Bornite	−1.6	−1.8		
SMS-17	Quartz vein type	Chalcopyrite	−1.2	−1.0		
SMS-7 *	Quartz vein type	Pyrite	−2.2	−3.4		
SMS-40 *	Quartz vein type	Molybdenite	−2.0	−3.9		
SMS-22 *	Quartz vein type	Molybdenite	−1.4	−2.8		
Y08	Cryptoexplosion breccia	Chalcopyrite	−0.5	−0.4		Ruan et al. [13]
Y17	Cryptoexplosion breccia	Chalcopyrite	−1.0	−0.9		
Y40-2	Cryptoexplosion breccia	Chalcopyrite	−1.4	−1.3		
Y40-2	Cryptoexplosion breccia	Chalcopyrite	−0.6	−0.5		
Y43	Cryptoexplosion breccia	Chalcopyrite	−0.2	−0.1		
Y61-2	Cryptoexplosion breccia	Chalcopyrite	−1.3	−1.2		
Y62-2	Cryptoexplosion breccia	Chalcopyrite	−0.5	−0.4		
Y63	Cryptoexplosion breccia	Chalcopyrite	−0.1	0.0		
Y66	Cryptoexplosion breccia	Chalcopyrite	−1.2	−1.1		
Y67-2	Cryptoexplosion breccia	Chalcopyrite	−1.0	−0.9		
Y68	Cryptoexplosion breccia	Chalcopyrite	−0.9	−0.8		
Y76-2	Cryptoexplosion breccia	Chalcopyrite	1.1	1.2		
Y12	Cryptoexplosion breccia	Molybdenite	−0.8	−1.8		
Y40-1	Cryptoexplosion breccia	Molybdenite	−0.4	−1.4		
Y62-1	Cryptoexplosion breccia	Molybdenite	0.2	−0.8		
SM156-1	Cryptoexplosion breccia	Chalcopyrite	−1.7	−1.6	Wang [14]	
SM156-2	Cryptoexplosion breccia	Chalcopyrite	−1.6	−1.5		
Mo-SP1	Cryptoexplosion breccia	Molybdenite	−2.5	−3.7		
Mo-SP2	Cryptoexplosion breccia	Molybdenite	−1.0	−2.2		
Mo-SP4	Cryptoexplosion breccia	Molybdenite	−2.0	−3.2		
Mo-SP6	Cryptoexplosion breccia	Molybdenite	−1.8	−3.0		
Mo-SP8	Cryptoexplosion breccia	Molybdenite	−1.9	−3.0		
Mo-SP3	Quartz vein type	Molybdenite	−1.6	−2.8		
Mo-SP5	Quartz vein type	Molybdenite	−1.9	−3.1		
Mo-SP7	Quartz vein type	Molybdenite	−2.0	−3.2		

* Temperature data come from Liu et al. [28].

5. Discussion

5.1. Age of Mineralization

Previous molybdenite Re–Os dating of the Shimensi tungsten mineralization had yielded diverse isochron ages, such as 139.2 ± 1.0 Ma [8], 143.7 ± 1.2 Ma [7], 145.1 ± 1.0 Ma [29], and 149.6 ± 1.4 Ma [15]. All of these data were obtained from the same laboratory, and thus the age differences may have been caused by the Re–Os decoupling in large molybdenite grains [30–34]. An alternative explanation for this wide molybdenite Re–Os age range may have been caused by a complex history of magmatism and mineralization at Shimensi. Muscovite $^{40}\text{Ar}/^{39}\text{Ar}$ dating is widely used to determine the timing of hydrothermal mineralization, particularly that related to tungsten deposits [16,35].

The closure temperature for argon isotope systematics in muscovite was determined to be 350 °C under rapid cooling [36] and 270 °C under slow cooling or extended reheating [37]. Recent experimental data [38] suggest that the retentivity of argon in muscovite is greater than previously thought, and muscovite closure temperature is substantially higher (e.g., 425 °C for cooling at 100 °C/Ma). At Shimensi, homogenisation temperatures of fluid inclusions in the mineralization-phase quartz (152 to 387 °C) [1,13,28] are clearly lower than the muscovite Ar–Ar closure temperatures and

no obvious overprinting exists in the argon age-spectrum plateau data, implying that the $^{40}\text{Ar}/^{39}\text{Ar}$ ages of the muscovite were not affected by later thermal disturbance. Therefore, the Ar-Ar plateau age reflects the timing of mineralization.

Our new precise muscovite Ar-Ar mineralization age (145.70 ± 0.90 Ma) is indistinguishable to the Re-Os isochron age (145.1 ± 1.0 Ma; [29]) and the zircon U-Pb ages for the ore-related granitoids, e.g., ca. 147.4 to 148.3 Ma (porphyritic biotite granite), 146.1 ± 0.6 Ma (fine-grained granite), and ca. 143.0 to 143.1 Ma (granite porphyry) [8]. This suggests that the granitoids at Shimensi were both spatially and temporally related to the tungsten mineralization.

5.2. Source of Sulfur

Sulfur isotopic compositions of metallic minerals ($\delta^{34}\text{S}$) and ore-forming fluids ($\delta^{34}\text{S}_{\Sigma\text{S}}$) can constrain the possible sources of sulfur and other metallogenic elements, and help in deciphering the metallogenic conditions [39]. The range of $\delta^{34}\text{S}$ is narrow among the different Shimensi ore and sulfide types (-3.0‰ to 1.1‰ ; Table 3). Other W deposits have similar S isotope values, namely the world-class Chinese deposits of Xihuashan ($\delta^{34}\text{S} -1.6\text{‰}$ – $+0.6\text{‰}$; [40]), Taoxikeng ($\delta^{34}\text{S} -2.3\text{‰}$ – $+0.1\text{‰}$; [41]), and Dengfuxian ($\delta^{34}\text{S} -1.4\text{‰}$ – $+0.1\text{‰}$; [42]) and the Panasqueira W deposit (Portugal) ($\delta^{34}\text{S} -0.91\text{‰}$ – $+2.03\text{‰}$; [43]). The absence of oxidised minerals (hematite) and sulphates in the hydrothermal veins indicate that reduced sulfur (H_2S) was the main sulfur species in the hydrothermal fluids [39]. $\delta^{34}\text{S}_{\text{H}_2\text{S}}$ values of the hydrothermal fluids were calculated using the mineral- H_2S equations from Ohmoto and Rye [39] (Table 3). Calculated sulfur isotopic compositions for the hydrothermal fluids reveal a narrow $\delta^{34}\text{S}_{\text{H}_2\text{S}}$ range (-4.5‰ to 1.2‰ , average -1.8‰), which is also consistent with a magmatic (\pm mantle) sulfur source (Figure 4) [39,44]. This further supports that the Shimensi ore-forming fluids were closely related to the late Mesozoic magmatism (ca. 143 to 148 Ma; [8]).

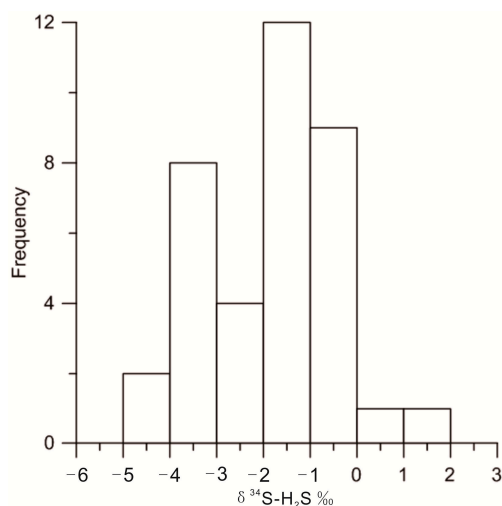


Figure 4. Histogram showing the sulfur isotopic composition of the Shimensi sulfides.

5.3. Source of Ore-Forming Fluids

The H-O isotopic compositions of the ore-forming fluid plot between the magmatic field and the global meteoric water line in the δD vs. $\delta^{18}\text{O}$ diagram (Figure 5), suggesting that magmatic fluids may have been important for the ore formation. These values are similar to those for several granite-related W deposits in the Nanling region of South China, Portugal, and Bolivia (Figure 5). The Shimensi ore-forming fluids were characterized by middle-low salinities, distinct from typical high temperature/salinity magmatic-derived fluids [45]. This implies that meteoric water may have contributed to the ore-forming fluids.

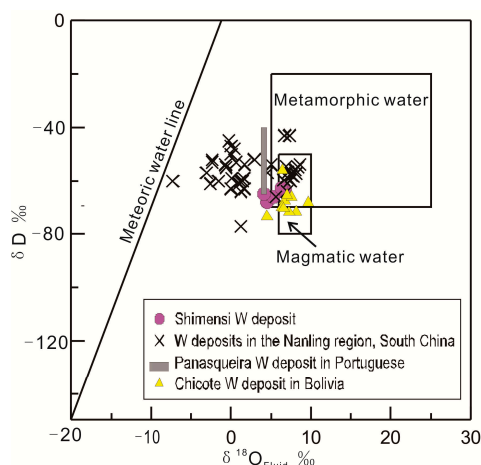


Figure 5. $\delta^{18}\text{O}$ vs. δD diagram of the Shimensi ore-forming fluids. Base map from Taylor [46].

5.4. Boiling or Mixing?

To further constrain the ore-forming processes, we performed quantitative modelling on the isotopic effects of cooling and mixing (Figure 6) using the quartz $\delta^{18}\text{O}$ data and the method of Wagner et al. [47,48]. The calculations used the mineral-water isotope fractionation equation of Matsuhisa et al. [49]. The equilibrium temperature was assumed to be 390 °C (the highest homogenisation temperature of fluid inclusions in quartz) [13]. For the calculations, we chose the end-member $\delta^{18}\text{O}$ values (+11.5‰) for the fluids in equilibrium with the magmatic end-member and $-7.5‰$ for the Mesozoic meteoric waters [50]. Temperatures of the meteoric end-member varied between 50 and 200 °C to reflect natural systems. The measured data do not fit the boiling/cooling curves, but do match the mixing trends (mass fractions of meteoric water: 0.2 to 0.4). Although there is evidence suggesting boiling (from fluid inclusions in quartz) had occurred, local boiling was probably less important for the hydrothermal evolution at Shimensi. We propose that magmatic-meteoric fluid mixing may have been the dominant mechanism for the tungsten mineralization.

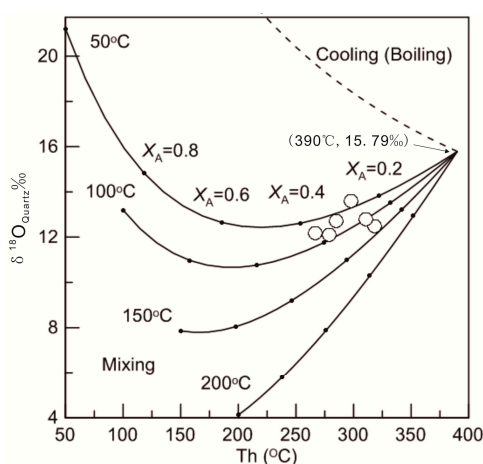


Figure 6. Diagram showing the influence of boiling and mixing on the oxygen isotopic composition of quartz precipitated at different temperatures. Numbers denote mass fraction of meteoric water.

5.5. Ore Deposition Processes

The high-grade Shimensi tungsten deposit suggests an effective ore-enrichment mechanism that may have caused tungsten super-saturation in the ore-forming fluids. Theoretical constraints indicate that NaHWO_4 , NaWO_4^- , HWO_4^- , and WO_4^{2-} were the dominant tungsten species in the ore-forming

fluids, which were likely formed under a moderately acidic pH and an oxygen fugacity (fO_2) close to the quartz–fayalite–magnetite (QFM) buffer [51]. The selective precipitation of wolframite and scheelite from the ore-forming fluids can be induced by an increase in fO_2 and pH and/or decrease in temperature and chloride ligand/ion activities [51]. The main mechanisms for initiating wolframite and scheelite precipitation are regarded to be boiling [52], fluid mixing [53,54], cooling [55], wall-rock alteration [56], and pressure decrease [57].

Mineralization-related wall-rock alteration (e.g., chlorite and greisen alterations) at Shimensi increases the fluid acidity and thus tungsten solubility [58]. Previous studies suggested that tungsten solubility is only weakly dependent on pressure and fO_2 [59]; therefore, cooling alone was unlikely to be enough for the high-grade tungsten ore formation.

Boiling would have oxidised the ore-forming fluids, decreased their temperature, significantly increased their pH due to the loss of acidic volatiles [48], and eventually promoted the precipitation of wolframite and scheelite. However, boiled fluid inclusions in quartz from Shimensi are rare [38]. Therefore, boiling may have occurred to a limited extent during the main ore-forming event. Moreover, ^{18}O enrichment and D depletion, which are common phenomena in boiling/vapour separation [59,60], are not apparent in the measured $\delta^{18}O$ and δD at Shimensi. Quantitative modelling of boiling and fluid mixing mechanisms also shows that boiling was unlikely a major process in the ore-forming fluid evolution. Instead, the occurrence of magmatic-meteoric fluid mixing is supported by the observed quartz $\delta^{18}O$ values. Fluid mixing may have decreased chloride concentration of the ore-forming fluids, leading to substantial tungsten solubility decrease and thus ore mineral precipitation [61].

5.6. Tectonic Setting of the Shimensi Deposit

Tungsten mineralization in the world took place within a large time span, although it peaked during Paleozoic and Mesozoic and sustained different deposit types (such as quartz vein-, skarn-, porphyry-, and disseminated-type) [62]. Paleozoic tungsten deposits are dominated by quartz vein type, followed by skarn type. By far the majority of the global tungsten resources (70%), represented mainly by vein-, skarn-, and porphyry-type, were formed in the Mesozoic [63]. The Panasqueira Mine (Portugal), a world-class W-Sn-Cu vein-type deposit that was formed during 296–292 Ma [37], is interpreted to have been associated with crust-mantle reaction [64]. Important tungsten mineralization formed during ca. 100–40 Ma in Japan [65], at ca. 210–140 Ma in Pan-African, and in ca. 96–90 Ma in North America [66] are all interpreted to have been associated with orogenic belts [67]. Tungsten deposits occurrences in Europe (340 to 320 Ma and 300 to 275 Ma) are related to extensional setting [67]. Based on contrastive analysis, one of the main factors that determine where the tungsten deposits are located is not so much geologic age, but proximity to tectonic setting [63,67].

South China is one of the most important W-polymetallic provinces in the world. Based on field relations and existing geochronological data, Mao et al. [68] proposed that the Mesozoic W-polymetallic mineralization in South China can be divided into three episodes: Late Triassic W-Sn-Nb-Ta mineralization (230–210 Ma), Late Jurassic W-Sn mineralization (160–150 Ma), and the Early Cretaceous Sn-W-Cu-Au mineralization (134–80 Ma). The Jurassic and Cretaceous mineralization may were formed under a continental arc environment, with widespread magmatism and related metallogenic events caused by the subduction of the Paleo-Pacific plate [68,69]. Previous studies considered that ca. 150–130 Ma was a relatively tranquil period of magmatism and mineralization in most of the South China Block [68]. The molybdenite Re-Os ages from the Shiweidong [7], Zhuxi [70] and Yangchuling [71] W-Cu deposits are 140.9 ± 3.6 Ma, 145.1 ± 1.5 Ma, and 146.4 ± 1.0 Ma, respectively. Therefore, Mao et al. [71] proposed that there was also a weak W-Cu mineralization epoch during 147–136 Ma in South China. It is generally accepted that continental crust extension occurred in South China during the Cretaceous, which was characterized by mafic dykes, pull-apart basins, and volcanic basins [12,69–71]. Crust-mantle interactions were important in forming the granite-related W polymetallic deposits of the Nanling and adjacent areas in the South China interior and were probably related to the magmatic and hydrothermal activities associated with lithospheric thinning

in South China. The Sr-Nd-Hf isotopic compositions indicate that the Shimensi W deposit-related granitoids are derived from the Neoproterozoic Shuangqiaoshan Group with mantle material [4,11]. As already stated, the Shimensi deposit belongs to the important Early Cretaceous (147–136 Ma) W-Cu mineralization event in South China, indicating that it occurred under lithospheric extension.

6. Conclusions

- (1) Muscovite $^{40}\text{Ar}/^{39}\text{Ar}$ age (145.70 ± 0.90 Ma) of the Shimensi deposit is consistent with the published zircon U-Pb age (143 to 148 Ma) of the ore-hosting granites, indicating a spatial-temporal link between them. The new age reported here confirms that the Shimensi tungsten deposit is part of a large Early Cretaceous (147–136 Ma) tungsten-polymetallic belt in South China.
- (2) A combination of $\delta^{34}\text{S}$, δD and $\delta^{18}\text{O}$ evidence shows that the ore fluids are mixtures of magmatic and meteoric waters.
- (3) Quantitative modelling of isotopic compositions of quartz shows that magmatic-meteoric fluid mixing was likely the main metallogenic mechanism for the wolframite and scheelite precipitation at Shimensi.

Acknowledgments: We are grateful to editors and anonymous reviewers for their thoughtful reviews. Their constructive and stimulating comments helped to significantly improve the manuscript. This research was financially supported by the National Basic Research Program of China (973 Program 2014CB440902) and the National Natural Science Foundation of China (41203034, 41303030, 41303030). Field work was supported by the No. 916 Geological Team, Jiangxi Province.

Author Contributions: Wen-Feng Wei contributed significantly to the data analyses and wrote the manuscript. Bing Yan helped perform the analysis with constructive discussions. Neng-Ping Shen conceived and designed the experiments and study design. Lei Liu drew the figures. Yong Zhang helped perform the literature search. Xin-Kui Xiang contributed to the data collection.

Conflicts of Interest: The authors declare no conflict of interest.

References

1. Gong, X.D.; Yan, G.S.; Ye, T.Z.; Zhu, X.Y.; Li, Y.S.; Zhang, Z.H.; Jia, W.B.; Yao, X.F. A Study of ore-forming fluids in the Shimensi tungsten deposit, Dahutang tungsten polymetallic ore field, Jiangxi Province, China. *Acta Geol. Sin.* **2015**, *89*, 822–835.
2. Jiang, S.Y.; Peng, N.J.; Huang, L.C.; Xu, Y.M.; Zhan, G.L.; Dan, X.H. Geological characteristic and ore genesis of the giant tungsten deposits from the Dahutang ore-concentrated district in northern Jiangxi Province. *Acta Petrol. Sin.* **2015**, *31*, 639–655. (In Chinese)
3. Chen, G.; Shu, L.; Shu, L.; Zhang, C.; Ouyang, Y. Geological characteristics and mineralization setting of the Zhuxi tungsten (copper) polymetallic deposit in the Eastern Jiangnan Orogen. *Sci. China Earth Sci.* **2016**, *59*, 803–823. [[CrossRef](#)]
4. Mao, Z.H.; Liu, J.J.; Mao, J.W.; Deng, J.; Zhang, F.; Meng, X.Y.; Xiong, B.K.; Xiang, X.K.; Luo, X.H. Geochronology and geochemistry of granitoids related to the giant Dahutang tungsten deposit, middle Yangtze River region, China: Implications for petrogenesis, geodynamic setting, and mineralization. *Gondwana Res.* **2015**, *28*, 816–836. [[CrossRef](#)]
5. Zhang, Z.H.; Geng, L.; Jia, W.B.; Gong, X.D.; Du, Z.Z.; Zhang, M.C. Regional geological characteristics study of tungsten-polymetallic ore field in Dahutang tungsten polymetallic deposit in north of Jiangxi. *China Min. Mag.* **2014**, *23*, 133–148. (In Chinese)
6. Cheng, Y.S.; Cao, X.M. Ore-forming Geological Conditions and Prospecting Potential in Dahutang W-Cu Polymetallic Ore District of North Jiangxi, China. *Acta Geol. Sin.* **2014**, *88*, 73–74. [[CrossRef](#)]
7. Feng, C.Y.; Zhang, D.Q.; Xiang, X.; Li, D.X.; Qu, H.; Liu, J.; Xiao, Y. Re-Os isotopic dating of molybdenite from the Dahutang tungsten deposit in northwestern Jiangxi Province and its geological implication. *Acta Petrol. Sin.* **2012**, *28*, 3858–3868. (In Chinese)

8. Mao, Z.H.; Cheng, Y.B.; Liu, J.J.; Yuan, S.D.; Wu, S.H.; Xiang, X.K.; Luo, X.H. Geology and molybdenite Re–Os age of the Dahutang granite-related veinlets-disseminated tungsten ore field in the Jiangxin Province, China. *Ore Geol. Rev.* **2013**, *53*, 422–433. [[CrossRef](#)]
9. Xiang, X.K.; Wang, P.; Sun, D.M.; Zhong, B. Isotopic geochemical characteristics of the Shimensi tungsten-polymetallic deposit in northern Jiangxi province. *Acta Geosci. Sin.* **2013**, *34*, 263–271. (In Chinese)
10. Xiang, X.K.; Wang, P.; Zhan, G.; Sun, D.M.; Zhong, B.; Qian, Z.; Tan, R. Geological characteristics of Shimensi tungsten polymetallic deposit in northern Jiangxi Province. *Miner. Depos.* **2013**, *32*, 1171–1187. (In Chinese)
11. Xiang, X.K.; Yin, Q.; Feng, C.Y.; Wang, H.; Liu, N.; Yu, Z. Elements and fluids migration regularity of granodiorite alteration zones in the Shimensi tungsten polymetallic deposit in northern Jiangxi and their constrain on mineralization. *Acta Geol. Sin.* **2015**, *89*, 1273–1287. (In Chinese)
12. Huang, L.C.; Jiang, S.Y. Highly fractionated S-type granites from the giant Dahutang tungsten deposit in Jiangnan Orogen, Southeast China: Geochronology, petrogenesis and their relationship with W-mineralization. *Lithos* **2014**, *202–203*, 207–226. [[CrossRef](#)]
13. Ruan, K.; Pan, J.Y.; Wu, J.Y.; Xiang, X.K.; Liu, W.Q.; Li, Z.S. Geochemical characteristics and ore genesis of the Shimensi cryptoexplosive breccia type tungsten deposit in Dahutang, Jiangxi Province. *Bull. Mineral. Petrol. Geochem.* **2015**, *34*, 633–641. (In Chinese)
14. Wang, P. Study on the Geological Characteristics, Ore-forming Fluid and Geochronology of the Shimensi Polymetallic Tungsten Deposit, Northern Jiangxi Province. Master's Thesis, Sinosteel Tianjin Geological Academy, Tianjing, China, 2013. (In Chinese)
15. Xiang, X.K.; Wang, P.; Sun, D.M.; Zhong, B. Re–Os isotopic age of molybdenite from the Shimensi tungsten polymetallic deposit in northern Jiangxi Province and its geological implications. *Geol. Bull. China* **2013**, *32*, 1824–1831. (In Chinese)
16. Hu, R.Z.; Wei, W.F.; Bi, X.W.; Peng, J.T.; Qi, Y.Q.; Wu, L.Y.; Chen, Y.W. Molybdenite Re–Os and muscovite $^{40}\text{Ar}/^{39}\text{Ar}$ dating of the Xihuashan tungsten deposit, central Nanling district, South China. *Lithos* **2012**, *150*, 111–118. [[CrossRef](#)]
17. Shu, L.S. An analysis of principal features of tectonic evolution in South China Block. *Geol. Bull. China* **2012**, *31*, 1035–1053. (In Chinese)
18. Xiang, X.K.; Liu, X.M.; Zhan, G.N. Discovery of Shimensi superlarge tungsten deposit and its prospecting significance in Dahutang area, Jiangxi Province. *Resour. Surv. Environ.* **2012**, *33*, 141–151. (In Chinese)
19. Sun, K.; Chen, B. Trace elements and Sr–Nd isotopes of scheelite: Implications for the W–Cu–Mo polymetallic mineralization of the Shimensi deposit, South China. *Am. Mineral.* **2017**, *102*, 1114–1128.
20. Wang, F.; Zhou, X.H.; Zhang, L.C.; Ying, J.F.; Zhang, Y.T.; Wu, F.Y.; Zhu, R.X. Late Mesozoic volcanism in the Great Xing'an Range (NE China): Timing and implications for the dynamic setting of NE Asia. *Earth Planet. Sci. Lett.* **2006**, *251*, 179–198. [[CrossRef](#)]
21. Koppers, A.A.P. ArArCALC—Software for $^{40}\text{Ar}/^{39}\text{Ar}$ age calculations. *Compu. Geosci.* **2002**, *28*, 605–619. [[CrossRef](#)]
22. Clayton, R.N.; Mayeda, T.K. The use of bromine pentafluoride in the extraction of oxygen from oxides and silicates for isotopic analysis. *Geochim. Cosmochim. Acta* **1963**, *27*, 43–52. [[CrossRef](#)]
23. Friedman, I. Deuterium content of natural waters and other substances. *Geochim. Cosmochim. Acta* **1953**, *4*, 89–103. [[CrossRef](#)]
24. Grassineau, N.V.; Matthey, D.P.; Lowry, D. Sulfur Isotope Analysis of Sulfide and Sulfate Minerals by Continuous Flow–Isotope Ratio Mass Spectrometry. *Anal. Chem.* **2001**, *73*, 220–225. [[CrossRef](#)] [[PubMed](#)]
25. Lee, J.Y.; Marti, K.; Severinghaus, J.P.; Kawamura, K.; Yoo, H.S.; Lee, J.B.; Kim, J.S. A redetermination of the isotopic abundances of atmospheric Ar. *Geochim. Cosmochim. Acta* **2006**, *70*, 4507–4512. [[CrossRef](#)]
26. Clayton, R.N.; O'Neil, J.; Mayeda, T. Oxygen isotope exchange between quartz and water. *J. Geophys. Res.* **1972**, *77*, 3057–3067. [[CrossRef](#)]
27. Rusk, B.G.; Reed, M.H.; Dilles, J.H. Fluid inclusion evidence for magmatic-hydrothermal fluid evolution in the porphyry copper-molybdenum deposit at Butte, Montana. *Econ. Geol.* **2008**, *103*, 307–334. [[CrossRef](#)]
28. Liu, L.; Yan, B.; Wei, W.F.; Yan, H.; Li, J.; Deng, X.W. Characteristics and significance of the fluid inclusions in quartz veins type ore bodies from Shimensi tungsten deposit, northern Jiangxi. *J. Miner. Petrol.* **2016**, *36*, 44–52. (In Chinese)

29. Ye, Z.Y.; Zhang, Z.Y.; Pan, X.F.; Peng, H.M. A study of the relationship of W-Cu-Mo mineralization features of the Shimensi ore district in northern Dahutang, Jiangxi Province. *Acta Petrol. Miner.* **2016**, *35*, 457–468. (In Chinese)
30. Stein, H.J.; Sundblad, K.; Markey, R.J.; Morgan, J.W.; Motuza, G. Re-Os ages for Archean molybdenite and pyrite, Kuittila-Kivisuo, Finland and Proterozoic molybdenite, Kabeliai, Lithuania: Testing the chronometer in a metamorphic and metasomatic setting. *Miner. Depos.* **1998**, *33*, 329–345. [[CrossRef](#)]
31. Stein, H.J.; Markey, R.J.; Morgan, J.W.; Hannah, J.L.; Scherstén, A. The remarkable Re-Os chronometer in molybdenite: How and why it works. *Terra Nova* **2001**, *13*, 479–486. [[CrossRef](#)]
32. Stein, H.; Scherstén, A.; Hannah, J.; Markey, R. Subgrain-scale decoupling of Re and ^{187}Os and assessment of laser ablation ICP-MS spot dating in molybdenite. *Geochim. Cosmochim. Acta* **2003**, *67*, 3673–3686. [[CrossRef](#)]
33. Selby, D.; Creaser, R.A. Macroscale NTIMS and microscale LA-MC-ICP-MS Re-Os isotopic analysis of molybdenite: Testing spatial restrictions for reliable Re-Os age determinations, and implications for the decoupling of Re and Os within molybdenite. *Geochim. Cosmochim. Acta* **2004**, *68*, 3897–3908. [[CrossRef](#)]
34. Li, C.; Qu, W.J.; Du, A.D. Decoupling of Re and Os and migration model of ^{187}Os in coarse-grained molybdenite. *Miner. Depos.* **2009**, *28*, 707–712. (In Chinese)
35. Peng, J.T.; Zhou, M.F.; Hu, R.Z.; Shen, N.P.; Yuan, S.D.; Bi, X.W.; Du, A.D.; Qu, W.J. Precise molybdenite Re-Os and mica Ar-Ar dating of the Mesozoic Yaogangxian tungsten deposit, central Nanling district, South China. *Miner. Depos.* **2006**, *41*, 661–669. [[CrossRef](#)]
36. Hames, W.E.; Bowring, S.A. An empirical evaluation of the argon diffusion geometry in muscovite. *Earth Planet. Sci. Lett.* **1994**, *124*, 161–169. [[CrossRef](#)]
37. Snee, L.W.; Sutter, J.F.; Kelly, W.C. Thermochronology of economic mineral deposits; dating the stages of mineralization at Panasqueira, Portugal, by high-precision $^{40}\text{Ar}/^{39}\text{Ar}$ age spectrum techniques on muscovite. *Econ. Geol.* **1988**, *83*, 335–354. [[CrossRef](#)]
38. Harrison, T.M.; Célérier, J.; Aikman, A.B.; Hermann, J.; Heizler, M.T. Diffusion of ^{40}Ar in muscovite. *Geochim. Cosmochim. Acta* **2009**, *73*, 1039–1051. [[CrossRef](#)]
39. Ohmoto, H.; Goldhaber, M.B. Sulfur and carbon isotopes. In *Geochemistry of Hydrothermal Ore Deposits*, 3rd ed.; Barnes, H.L., Ed.; John Wiley Sons: New York, NY, USA, 1997; pp. 517–611.
40. Wei, W.F.; Hu, R.Z.; Bi, X.W.; Peng, J.T.; Su, W.C.; Song, S.Q.; Shi, S.H. Infrared microthermometric and stable isotopic study of fluid inclusions in wolframite at the Xihuashan tungsten deposit, Jiangxi province, China. *Miner. Depos.* **2012**, *47*, 589–605. [[CrossRef](#)]
41. Cai, Y.; Ma, D.S.; Lu, J.J.; Huang, H.; Zhang, R.Q.; Qu, W.J. Re-Os geochronology and S isotope geochemistry of Dengfuxian tungsten deposit, Hunan Province, China. *Acta Petrol. Sin.* **2012**, *28*, 3798–3808. (In Chinese)
42. Song, S.Q.; Hu, R.Z.; Bi, X.W.; Wei, W.F.; Shi, S.H. Hydrogen, oxygen and sulfur isotope geochemical characteristics of Taoxikeng tungsten deposit in Chongyi County, Southern Jiangxi Province. *Miner. Depos.* **2011**, *30*, 1–10. (In Chinese)
43. Kelly, W.C.; Rye, R.O. Geologic, fluid inclusion, and stable isotope studies of the tin-tungsten deposits of Panasqueira, Portugal. *Econ. Geol.* **1979**, *74*, 1721–1822. [[CrossRef](#)]
44. Rye, R.O. The evolution of magmatic fluids in the epithermal environment: The stable isotope perspective. *Econ. Geol.* **1993**, *88*, 733–752. [[CrossRef](#)]
45. Audetat, A.; Pettke, T.; Heinrich, C.A.; Bodnar, R.J. Special Paper: The Composition of Magmatic-Hydrothermal Fluids in Barren and Mineralized Intrusions. *Econ. Geol.* **2008**, *103*, 877–908. [[CrossRef](#)]
46. Taylor, H. Oxygen and hydrogen isotope relationships in hydrothermal mineral deposits. In *Geochemistry of Hydrothermal ore Deposits*, 3rd ed.; Barnes, H.L., Ed.; John Wiley Sons: New York, NY, USA, 1997; pp. 229–302.
47. Wagner, T.; Mlynarczyk, M.S.J.; Williams-Jones, A.E.; Boyce, A.J. Stable isotope constraints on ore formation at the San Rafael tin-copper deposit, Southeast Peru. *Econ. Geol.* **2009**, *104*, 223–248. [[CrossRef](#)]
48. Wagner, T.; Williams-Jones, A.E.; Boyce, A.J. Stable isotope-based modeling of the origin and genesis of an unusual Au-Ag-Sn-W epithermal system at Cirotan, Indonesia. *Chem. Geol.* **2005**, *219*, 237–260. [[CrossRef](#)]
49. Matsuhisa, Y.; Goldsmith, J.R.; Clayton, R.N. Oxygen isotopic fractionation in the system quartz-albite-anorthite-water. *Geochim. Cosmochim. Acta* **1979**, *43*, 1131–1140. [[CrossRef](#)]

50. Zhang, L.G. *Retrogenic and Minerogenetic Theories and Prospecting: Stable Isotopic Geochemistry of Main Type ore Deposits and Granitoids of China*, 1st ed.; Press of Beijing University of Technology: Beijing, China, 1989; pp. 49–65. (In Chinese)
51. Wood, S.A.; Samson, I.M. The Hydrothermal geochemistry of tungsten in granitoid environments: I. Relative solubilities of ferberite and scheelite as a function of T, P, pH, and m_{NaCl} . *Econ. Geol.* **2000**, *95*, 143–182. [[CrossRef](#)]
52. Graupner, T.; Kempe, U.; Dombon, E.; Pätzold, O.; Leeder, O.; Spooner, E.T.C. Fluid regime and ore formation in the tungsten-(yttrium) deposits of Kyzyltau (Mongolian Altai): Evidence for fluid variability in tungsten-tin ore systems. *Chem. Geol.* **1999**, *154*, 21–58. [[CrossRef](#)]
53. Beuchat, S.; Moritz, R.; Pettke, T. Fluid evolution in the W-Cu-Zn-Pb San Cristobal vein, Peru: Fluid inclusion and stable isotope evidence. *Chem. Geol.* **2004**, *210*, 201–224. [[CrossRef](#)]
54. Moura, A.; Dória, A.; Neiva, A.M.R.; Leal Gomes, C.; Creaser, R.A. Metallogensis at the Carris W-Mo-Sn deposit (Gerês, Portugal): Constraints from fluid inclusions, mineral geochemistry, Re-Os and He-Ar isotopes. *Ore Geol. Rev.* **2014**, *56*, 73–93. [[CrossRef](#)]
55. Xi, B.B.; Zhang, D.H.; Zhou, L.M.; Zhang, W.H.; Wang, C. Characteristics of ore-forming fluid evolution in Dajishan tungsten deposit, Quannan county, Jiangxi. *Acta Geol. Sin.* **2008**, *82*, 956–966. (In Chinese)
56. Gong, Q.J.; Yu, C.W.; Zhang, R.H. Physical chemistry study on the ore-forming process of Shizhuyuan tungsten-polymetallic deposit. *Earth Sci. Front.* **2004**, *11*, 617–625. (In Chinese)
57. Polyá, D.A. Chemistry of the main-stage ore-forming fluids of the Panasqueira W-Cu(Ag)-Sn deposit, Portugal: Implications for models of ore genesis. *Econ. Geol.* **1989**, *84*, 1134–1152. [[CrossRef](#)]
58. Ding, W.K. Research of Alteration Zone in Shimensi Tungsten Polymetallic Deposit. Master's Thesis, East China University of Technology, Fuzhou, China, 2016. (In Chinese)
59. Koděra, P.; Lexa, J.; Rankin, A.H.; Fallick, A.E. Epithermal gold veins in a caldera setting: Banská Hodruša, Slovakia. *Miner. Depos.* **2005**, *39*, 921–943. [[CrossRef](#)]
60. Yoo, B.; Lee, H.; White, N. Mineralogical, fluid inclusion, and stable isotope constraints on mechanisms of ore deposition at the Samgwang mine (Republic of Korea)—A mesothermal, vein-hosted gold-silver deposit. *Miner. Depos.* **2010**, *45*, 161–187. [[CrossRef](#)]
61. Hulsbosch, N.; Boiron, M.C.; Dewaele, S.; Muchez, P. Fluid fractionation of tungsten during granite-pegmatite differentiation and the metal source of peribatholithic W quartz veins. Evidence from the Karagwe-Ankole Belt (Rwanda). *Geochim. Cosmochim. Acta* **2016**, *175*, 299–318. [[CrossRef](#)]
62. Shi, H.Z.; Lin, F.C.; Zhang, L.K. Spatio-temporal distribution and current state of the research of the tungsten deposits: An overview. *Sediment. Geol. Tethyan Geol.* **2009**, *29*, 90–95. (In Chinese)
63. Werner, A.B.T.; Sinclair, W.D.; Amey, E.B. *International Strategic Mineral Issues Summary Report—Tungsten*; U.S. Geological Survey Circular 930-O; United States Government Printing Office: Washington, DC, USA, 1998; pp. 1–71.
64. Burnard, P.G.; Polyá, D.A. Importance of mantle derived fluids during granite associated hydrothermal circulation: He and Ar isotopes of ore minerals from Panasqueira. *Geochim. Cosmochim. Acta* **2004**, *68*, 1607–1615. [[CrossRef](#)]
65. Sato, K. Sedimentary Crust and Metallogeny of Granitoid Affinity: Implications from the Geotectonic Histories of the Circum-Japan Sea Region, Central Andes and Southeastern Australia. *Resour. Geol.* **2012**, *62*, 329–351. [[CrossRef](#)]
66. Hart, C.J.R.; Mair, J.L.; Goldfarb, R.J.; Groves, D.I. Source and redox controls on metallogenic variations in intrusion-related ore systems, Tombstone-Tungsten Belt, Yukon Territory, Canada. *Trans. Royal Soc. Edinb. Earth Sci.* **2004**, *95*, 339–356. [[CrossRef](#)]
67. Romer, R.L.; Kroner, U. Phanerozoic tin and tungsten mineralization—Tectonic controls on the distribution of enriched protoliths and heat sources for crustal melting. *Gondwana Res.* **2016**, *31*, 60–95. [[CrossRef](#)]
68. Mao, J.W.; Cheng, Y.B.; Chen, M.H.; Pirajno, F. Major types and time-space distribution of Mesozoic ore deposits in South China and their geodynamic settings. *Miner. Depos.* **2013**, *48*, 267–294.
69. Liu, P.; Mao, J.W.; Cheng, Y.B.; Yao, W.; Wang, X.Y.; Hao, D. An Early Cretaceous W-Sn deposit and its implications in southeast coastal metallogenic belt: Constraints from U-Pb, Re-Os, Ar-Ar geochronology at the Fei'e'shan W-Sn deposit, SE China. *Ore Geol. Rev.* **2017**, *81*, 112–122. [[CrossRef](#)]

70. Pan, X.F.; Hou, Z.Q.; Li, Y.; Chen, G.H.; Zhao, M.; Zhang, T.F.; Zhang, C.; Wei, J.; Kang, C. Dating the giant Zhuxi W-Cu deposit (Taqian-Fuchun Ore Belt) in South China using molybdenite Re-Os and muscovite Ar-Ar system. *Ore Geol. Rev.* **2017**, *86*, 719–733. [[CrossRef](#)]
71. Mao, J.W.; Xiong, B.K.; Liu, J.; Pirajno, F.; Cheng, Y.B.; Ye, H.S.; Song, S.W.; Dai, P. Molybdenite Re/Os dating, zircon U-Pb age and geochemistry of granitoids in the Yangchuling porphyry W-Mo deposit (Jiangnan tungsten ore belt), China: Implications for petrogenesis, mineralization and geodynamic setting. *Lithos* **2017**, *286–287*, 35–52. [[CrossRef](#)]



© 2017 by the authors. Licensee MDPI, Basel, Switzerland. This article is an open access article distributed under the terms and conditions of the Creative Commons Attribution (CC BY) license (<http://creativecommons.org/licenses/by/4.0/>).